Unravelling the Stability Stressors of Atomically Dispersed Fe–N–C Oxygen Reduction Catalysts

Xiaohong Xie, Boyang Li, Pan Xu, Moulay Tahar Sougrati, Ricardo Garcia-Serres, David Cullen, A. Jeremy Kropf, Fan Xia, Miao Song, Sulay Saha, et al.

Unravelling the Stability Stressors of Atomically Dispersed Fe-N-C Oxygen Reduction Catalyst

Xiaohong Xie,[§] Boyang Li,[§] Pan Xu,[§] Moulay Tahar Sougrati, Ricardo Garcia-Serres, David A. Cullen, A. Jeremy Kropf, Fan Xia, Miao Song, Sulay Saha, Yachao Zeng, Mark H. Engelhard, Mark E. Bowden, Hanguang Zhang, Litao Yan, Teresa Lemmon, Xiaohong S. Li, Ulises Martinez, Yingwen Cheng, Gang Wu, Piotr Zelenay, Vijay Ramani, Deborah J. Myers, Frédéric Jaouen,* Lijun Yang,* Guofeng Wang,* and Yuyan Shao*

ABSTRACT

Enhancing catalytic stability of Fe-N-C catalysts for cathodic oxygen reduction in proton exchange membrane fuel cells necessitates an in-depth understanding of their degradation mechanisms. This study identifies key stressors affecting Fe-N-C catalysts stability, specifically acidic-environment, oxygen (O_2), and reactive oxygen species (ROS). Through ex situ/operando experiments, we show that the oxidation of local carbon by acidic-environment + O_2 + ROS, along with the demetallation of catalytic FeN_xC_y sites by O_2 or O_2 + ROS, are the primary factors responsible for the initial fast degradation of Fe-N-C catalysts. The demetallation of FeN_xC_y sites, influenced by O_2, in particular by O_2 + ROS, leads to the subsequent gradual degradation of Fe-N-C. Notably, FeN_4C_{12} type active sites are more susceptible to demetallation than FeN_4C_{10} type sites in O_2 or O_2 + ROS. Our findings indicate that, besides constructing more stable FeN_xC_y sites, preventing local carbon oxidation and scavenging of ROS are all critical for maintaining stability of Fe-N-C catalysts.

1. INTRODUCTION

Electrocatalysis of the oxygen reduction reaction (ORR) is a cornerstone of proton exchange membrane fuel cells (PEMFCs).[1] The harsh operating environment in PEMFCs demands catalysts with both high activity and stability and, due to these requirements, platinum group metals (PGMs) have been the predominant catalysts of choice.[2, 3] Nevertheless, the high costs and low reserves of PGMs preclude their large-scale application.[4] PGM-free Fe-N-C, which are typically synthesized through pyrolysis of Fe-containing polymers[5, 6] or metal-organic-frameworks (e.g., ZIF-8),[7-9] have achieved decent beginning-of-life activity and are among the most promising alternatives to PGM catalysts. However, Fe-N-C suffers significantly from insufficient stability when catalyzing ORR in acidic conditions.[10]

The performance of PEMFCs with Fe-N-C cathodes often degrades by ~40-80% within only tens of hours of operation at practical cell voltages exceeding 0.6 V.[11, 12] This degradation typically features a rapid initial loss in the first few hours, followed by a slower, more gradual decline over the remaining operational time.[13-15] The chemical and structural degradation of Fe-N-C is primarily attributed to catalyst carbon corrosion,[16-18] FeN_xC_y active sites demetallation,[19-23] and FeN_xC_y sites deactivation by surface N/O functionalities.[24-26] Additionally, reactive oxygen species (ROS), such as $^{\bullet}O$, $^{\bullet}OH$, and $^{\bullet}OOH$ radicals (the dot denotes an unpaired electron), contribute to the degradation process.[26, 27] The attack of Fe-N-C by ROS triggers an increased production of hydrogen peroxide (H_2O_2) during the ORR by FeN_xC_y active sites,[21, 26] which subsequently increases the ROS levels,[28] creating a positive feedback loop that deteriorates the Fe-N-C performance and ultimately leads to partial or complete destruction of FeN_xC_y sites. These degradation processes are believed to occur concurrently or be

interdependent, making it challenging to identify the key factors that dictate Fe-N-C degradation and spanning their entire lifetime.

One recent breakthrough has quantitatively identified Fe dissolution as the primary cause of Fe-N-C activity decay under temperature/gas-controlled gas-diffusion electrode conditions.[29] End-of-test analyses of Fe-N-C showed that different types of FeN_xC_y active sites suffer demetallation with different rates and the rapid demetallation of the FeN_4C_{12} sites (denoted as S1) is responsible for the fast degradation of Fe-N-C.[20] This finding suggests that the rational catalyst design should focus on increasing the density of more durable FeN_xC_y active sites, specifically the FeN_4C_{10} type (denoted as S2)).[30, 31] However, controversy arises since a number of studies have shown that Fe-N-C still degrades rapidly even when stable S2 sites constitute relatively a high proportion of >40% (Table S1). Moreover, the mechanism for S1 sites exhibit much easier demetallation than S2 sites also remains unclear. Therefore, enhancing the stability of Fe-N-C catalysts requires more in-depth understanding of the underlying degradation mechanisms. Here, we delineate the degradation of a highly active atomically dispersed Fe-N-C catalyst and its dependence on the key stability stressors associated with the ORR.

2. RESULTS AND DISCUSSION

2.1. Atomically Dispersed Fe-N-C Catalyst

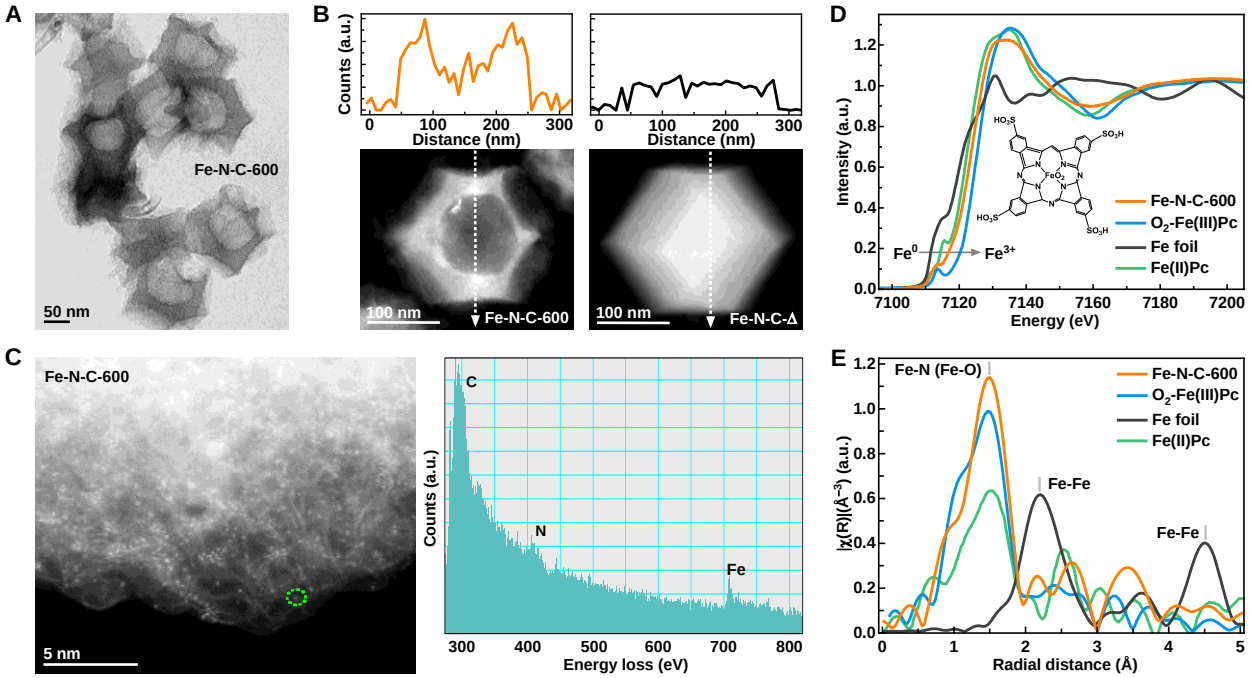

Figure 1 (A) Bright-field STEM image of Fe-N-C-600 catalyst. (B) Dark-field STEM images and the corresponding energy dispersive X-ray spectroscopy line scanning profiles of Fe-N-C-600 and counterpart Fe-N-C-Δ. (C) HAADF-STEM image and the corresponding EELS spectrum to verify the Fe, N, and C co-existence at the atomic level in Fe-N-C-600. (D) and (E) Fe K-edge XANES (D) and Fourier-transformed EXAFS (E) spectra of Fe-N-C-600, Fe foil, Fe(II)Pc, O_2-Fe(III)Pc, and with the O_2-Fe(III)Pc structure given in the inset of (D).

We first developed a single atomic Fe-N-C catalyst characterized by a high density of FeN_xC_y site. The synthesis involved the pyrolysis of a $Fe(acac)_3$@ZIF-8 (acac: acetylacetonate) precursor[21] (Figures S1 and S2) under a novel continuous two-step pyrolysis protocol: first in ammonia (NH_3) (no gas flow) at temperatures below 600 °C and then in argon (Ar) (with gas flow) at temperatures above 600 °C. This resultant material is designated as Fe-N-C-600 and 600

is the optimal NH_3-to-Ar switching temperature (see Methods in the Supporting Information for details, Figure S2). The pre-treatment in NH_3 led to not only the formation of a porous hollow structure but also a relative increase in Fe content of Fe-N-C-600 compared to a catalyst (Fe-N-C-Δ) that was synthesized with the same method but with only Ar (Figures 1A,B, S2, S3, and Table S2). Atomic-scale High-angle annular dark-field scanning transmission electron microscopy (HAADF-STEM) characterization of Fe-N-C-600 reveals a high density of atomically dispersed Fe sites (Figures 1C and S4); X-ray diffraction verifies the absence of metallic/oxide/carbide phase of Fe at macroscopic scale (Figure S1). The electron energy loss point spectrum (EELS) (Figure 1C), obtained from an single Fe atom within Fe-N-C-600 (cycled in green in Figure 1C), shows the co-location of Fe, N, and C, affirming the formation of FeN_xC_y coordination (Figure S4).[5] In contrast, the counterpart Fe-N-C-Δ catalyst retained the dense rhombic dodecahedron structure of ZIF-8 precursor (Figure S3) and with lower density of single Fe atoms (Figure S5). This highlights the significant role of the NH_3 pre-treatment in synthesizing the Fe-N-C-600 catalyst.

More evidence of FeN_xC_y and insights into the local coordination environment were obtained from X-ray absorption spectroscopy (XAS).[32] As shown in Figure 1D, the X-ray absorption near-edge structure (XANES) spectrum indicates that the adsorption threshold position of Fe-N-C-600 located between Fe phthalocyanine (Fe(II)Pc) and Fe phthalocyanine-4,4′,4″,4‴-tetrasulfonic acid (compound with an O_2 axial ligand atop the Fe atom) (O_2-Fe(III)Pc, inset of Figure 1D), implying that the valence of Fe in Fe-N-C-600 is situated between +2 and +3. This further suggests that Fe-N-C-600 contains a mixture of $Fe(II)N_xC_y$ and $Fe(III)N_xC_y$ sites.[14, 33] Comparative analysis of our experimental XANES spectrum with the XANES simulations of Zitolo et al.[34] suggests that Fe-N-C-600 comprised mainly the $Fe(III)N_4C_{12}$ (S1) and $Fe(II)N_4C_{10}$ (S2) sites (Figure S6). The Fourier-transformed extended X-ray absorption fine structure (EXAFS) spectrum of Fe-N-C-600 further shows solely the Fe-N/Fe-O interactions with a bond length (~1.49 Å) typical of FeN_xC_y sites and no evidence of Fe-Fe scattering (Figures 1E and S7). This indicates that Fe is atomically dispersed, which, combined with the XANES signature, confirms that $FeN_4(O_x)C_y$ is the dominant Fe species in Fe-N-C-600. The presence of S1 (~56%) and S2 (~30%) sites in the catalyst is further confirmed by ^{57}Fe Mössbauer spectroscopic characterization (Figure S8 and Table S3). Notably, the structure and chemistry (in terms of porosity (Figure S9), size, Fe content/dispersion, type/ratio of FeN_xC_y sites, etc.) of our Fe-N-C-600 catalyst are similar to that of majority single atomic Fe-N-C catalysts in the literature,[7, 20, 30, 34-38] making it a representative catalyst for studying the degradation of Fe-N-C catalysts with the ORR.

The ORR activity of catalysts was first evaluated using a rotating ring-disk electrode (RRDE) in O_2-saturated 0.5 M H_2SO_4. Fe-N-C-600 exhibits high activity with an onset potential (E_{on}, E at a current density of –0.1 mA cm^{-2}) of about 1.0 V (versus the reversible hydrogen electrode (RHE)) and a half wave-potential ($E_{1/2}$) of approximately 0.87 V (Figure 2A). This ORR activity is among the best reported for PGM-free ORR catalysts in acidic conditions.[8, 14, 15, 31] In contrast, Fe-N-C-Δ exhibited a lower performance, with an E_{on} of about 0.91 V and an $E_{1/2}$ around 0.82 V, significantly trailing behind Fe-N-C-600. The NH_3 treatment at 600 °C was found to maximize the ORR activity, correlating with an increase in atomically dispersed Fe content (Figures S3 and S10). RRDE results also showed that the H_2O_2 yield for Fe-N-C-600 was below 2% at a loading of 600 μg cm^{-2}, rising only slightly to 3-5% at an ultra-low loading of 37.5 μg cm^{-2} (Figure S10). This confirms that Fe-N-C-600 predominantly follows a four-electron (4 e$^-$) ORR pathway.[39, 40]

Fe-N-C-600 was then evaluated in a PEMFC cathode. Tested under 1.0 bar H_2/O_2 condition,[41] the cell yielded a high current density of nearly 46 mA cm^{-2} (mass activity of about 11.6 A g^{-1}) at an of 0.9 $V_{iR\text{-}free}$ (internal resistance-compensated voltage) (Figures 2B and S11). This performance surpasses the U.S. Department of Energy's 2025 activity target of 44 mA cm^{-2} and is among the highest reported for Fe-N-C catalysts in PEMFCs, which are in the range of 15-51 mA cm^{-2} (mass activities between 5-13 A g^{-1}) (Table S4). Under more practical 1.0 bar H_2/air condition, the cell generated a peak power density of about 570 mW cm^{-2} and a current density of approximately 150 mA cm^{-2} at 0.8 V (Figure 2C). These values are among the highest reported for PGM-free cathode catalysts (Table S4). We attribute this high ORR performance to the combination of a high density and high accessibility of FeN_xC_y site in the catalyst. Fe-N-C-600 exhibited significant porosity, as evidenced by nitrogen (N_2) sorption isotherms (Figure S9), which indicated a substantial presence of macropores greater than 50 nm. Cross sectional scanning electron microscopy images of the Fe-N-C-600 catalyst layer supports our hypothesis (Figures S12 and S13), suggesting efficient mass transport under H_2/air PEMFC condition. The uniform distribution of F (F of the Nafion® ionomer) throughout Fe-N-C-600 catalyst layer, as observed by elemental mapping in Figures S12 and S13, further suggests a strong interaction between catalyst and Nafion® ionomer (Figure S7), promoting to extended triple-phase boundaries and enhanced proton accessibility to the FeN_x active sites and contributing to effective ORR catalytic activity.[13]

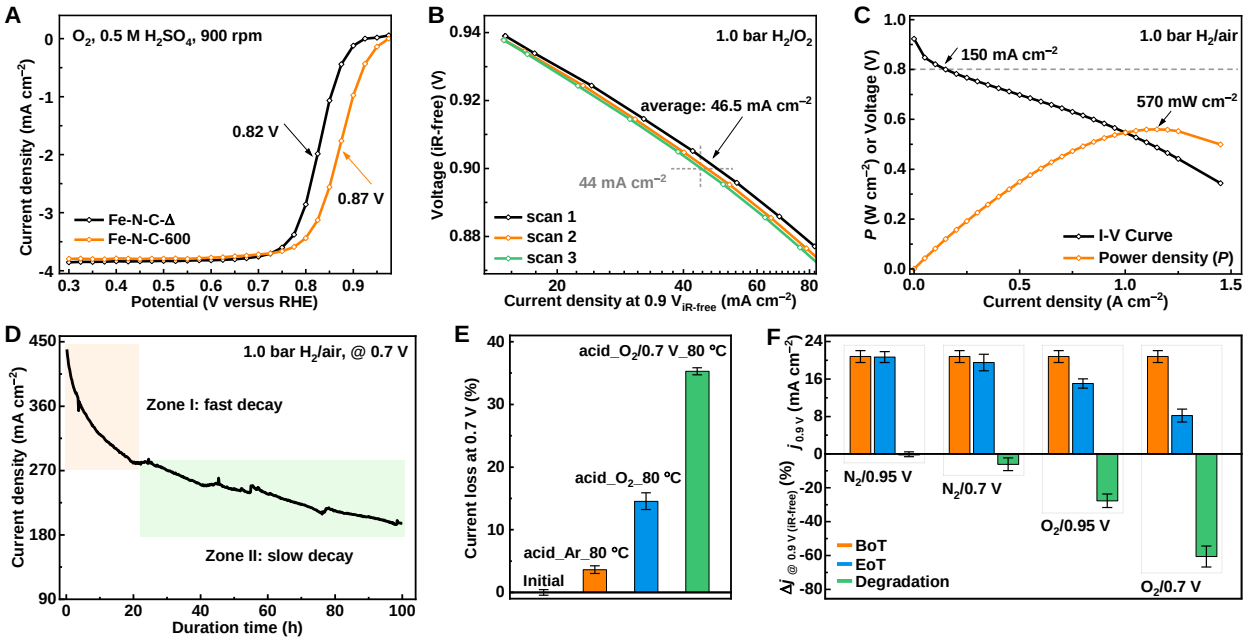

Figure 2 (A) Steady-state ORR polarization curves of Fe-N-C-Δ and Fe-N-C-600 catalysts. 600 µg cm^{-2} loading, 0.5 M H_2SO_4, O_2, 25 °C, and 900 rpm RDE rotation speed. (B) The first three polarization curves of Fe-N-C-600 catalyst in PEMFC in 1.0 bar H_2/O_2. Cathode: 4.0 mg $cm^{-2}_{Fe\text{-}N\text{-}C\text{-}600}$, anode: 0.2 mg cm^{-2}_{Pt}, 5.0 cm^2 membrane electrode assembly (MEA), Gore membrane, 80 °C, and 100% relative humidity (RH). (C) and (D) H_2/air PEMFC activity (C) and 100-hour stability (D) of Fe-N-C-600 catalyst. Cathode: 2.5 mg $cm^{-2}_{Fe\text{-}N\text{-}C\text{-}600}$, anode: 0.1 mg cm^{-2}_{Pt}, 5.0 cm^2 MEA, NR211 membrane, 1.0 bar H_2/air, 80 °C, and 100% RH. (E) ORR activity (0.7 V) loss for Fe-N-C-600 catalyst after the electrode being subjected to immersion in acid_Ar_80 °C, acid_O_2_80 °C, and acid_O_2/0.7 V_80 °C. (F) Determination of ORR activity at 0.9 $V_{iR\text{-}free}$ before and after potential hold at 0.7 V and 0.95 V in PEMFCs in O_2 or N_2. Cathode: 2.5 mg $cm^{-2}_{Fe\text{-}N\text{-}C\text{-}600}$, anode: 0.1 mg cm^{-2}_{Pt}, 5.0 cm^2 MEA, NR211

membrane, 80 °C, and 100% RH. The error bars refer to standard deviation (S.D.) for two independent experiments performed under given conditions.

2.2. Catalyst Stability

RRDE stability test shows that Fe-N-C-600 catalyst experienced a loss of nearly 40 mV in its $E_{1/2}$ and a 2.5-fold increase in H_2O_2 yield following a standard accelerated stability test (ADT).[41] This test involved 30,000 cycles between 0.6 V and 1.0 V (versus RHE) at 25 °C in O_2-saturated 0.5 M H_2SO_4 (Figure S14); H_2/air PEMFC test reveals that the Fe-N-C-600 cathode exhibits initial rapid activity loss (denoted as fast decay Zone I), followed by a significant and sustained activity decay (noted as slow decay Zone II) during a 100-hour hold at a cell voltage of 0.7 V (Figure 2D). Such degradations are common-observed for highly active single atomic Fe-N-C catalysts (Figure S15). We then designed both ex situ and operando experiments to identify the key stability stressors and differentiate their effect on Fe-N-C.

To identify the stability stressors affecting Fe-N-C catalyst, we first carried out RDE stability tests under various conditions of Ar, O_2, and O_2 at a 0.7 V voltage (Figure S16). We used a catalyst loading of 37.5 μg cm^{-2} as this low loading facilitates fast mass transport, maximizes the utilization of FeN_xC_y catalytic sites, and allows H_2O_2 to easily diffuse away from the RDE. This significantly minimizes the influence of ROS (H_2O_2 + O radicals) on the stability evaluation of Fe-N-C under these conditions. As shown in Figure 2E, Fe-N-C-600 electrode shows minimal degradation after a 10-hour immersion in Ar-saturated H_2SO_4 and at 80 °C (labelled acid_Ar_80 °C), indicating that FeN_xC_y in Fe-N-C-600 is stable under such a condition. The degradation, however, increased after immersion in oxygenated H_2SO_4 (acid_O_2_80 °C) and increased even more with ORR occurred under the same condition (acid_O_2/0.7 V_80 °C). This shows that O_2 promotes the degradation of Fe-N-C, and the presence of O_2 at 0.7 V further accelerates this process. In this scenario, the ORR not only increases O_2 absorption[42, 43] but also produces ORR intermediates (e.g., *OOH, *OH, and *O (the asterisk denotes the adsorption site)), which can further contribute to the degradation while minimally affecting the ROS levels. Our PEMFC stability tests at varied cathode catalyst loadings further reveal that ROS degrades Fe-N-C catalysts (Figures S16-20).[27, 44-46]

We further studied key stability stressors affecting Fe-N-C catalyst under PEMFC conditions, including the acidic-environment (i.e., acidic and inert conditions at about 80 °C), O_2 (both physi- and chemisorbed), and ROS (radicals generated from H_2O_2 and oxygen intermediates produced by ORR). The tests involved a voltage-hold of Fe-N-C-600 cathode under N_2 or O_2 at a practical cell voltage of 0.7 V or near open circuit voltage of 0.95 V (see Methods in the Supporting Information for details). As shown in Figure 2F, after testing under N_2 at 0.7 or 0.95 V (i.e., acidic-environment), we observed minimal degradation in ORR activity, measured by a negligible change in the current density (Δj) at 0.9 $V_{iR\text{-}free}$ under 1.0 bar H_2/O_2. This confirms that the FeN_xC_y sites in Fe-N-C-600 are inherently stable under these conditions. Moreover, the degradation was found to be voltage or potential-independent under these conditions (Figures S21 and S22). Under O_2 at 0.95 V (i.e., O_2), however, the Δj decreased by 28%, showing that O_2 adsorption contributes to Fe-N-C degradation, even with no or very limited ORR occurring. Under O_2 at 0.7 V (O_2 + ROS), Δj exhibited a larger decline of 63%, indicating that the combined effects of O_2 and ROS significantly accelerate the degradation of Fe-N-C.

To investigate the structural changes of Fe-N-C-600 with the stability stressors, we performed ex situ experiments, where the catalyst was treated under three conditions: acid with Ar saturation at 80 °C for 2 hours (catalyst after treatment is noted as C_1), acid with O_2 at 80 °C

for 2 hours (C_2), and acid with O_2 and H_2O_2 at 80 ℃ for 2 hours (C_3) (see Methods in the Supporting Information for details). These conditions were specifically designed to mimic those of the aforementioned in operando conditions of acidic-environment, O_2, and O_2 + ROS, respectively. The loss of the ORR activity (kinetic current density at 0.85 V ($\Delta j_{k,\ 0.85\ V}$)) and turnover frequency (TOF), as well as the change in Fe content (Δm) of the treated catalysts (i.e., C_1, C_2, and C_3) versus the pristine catalyst, were determined with RDE and inductively coupled plasma optical emission spectroscopy (ICP-OES), respectively. C_2 and C_3 were further characterized by ^{57}Fe Mössbauer spectroscopy.

RDE test reveals that the Δj_k for C_1 is –20% (Figures 3A and S23). This activity decay aligns well with the results from in situ RDE and PEMFC stability tests and is likely attributed to the loss of very limited amount of acid-unstable FeN_xC_y sites (resulting from Fe dissolution in H_2SO_4),[16, 20] decrease of TOF of remaining FeN_xC_y sites due to mild (i.e., reversible) oxidation of local carbon of FeN_xC_y sites,[26] or a combination of both. For C_2, Δj_k increases to –59%, and for C_3, it reaches –90%. These results confirm that the exposure to O_2 and in particular to O_2 with ROS during the ex situ treatments significantly exacerbate catalyst degradation.

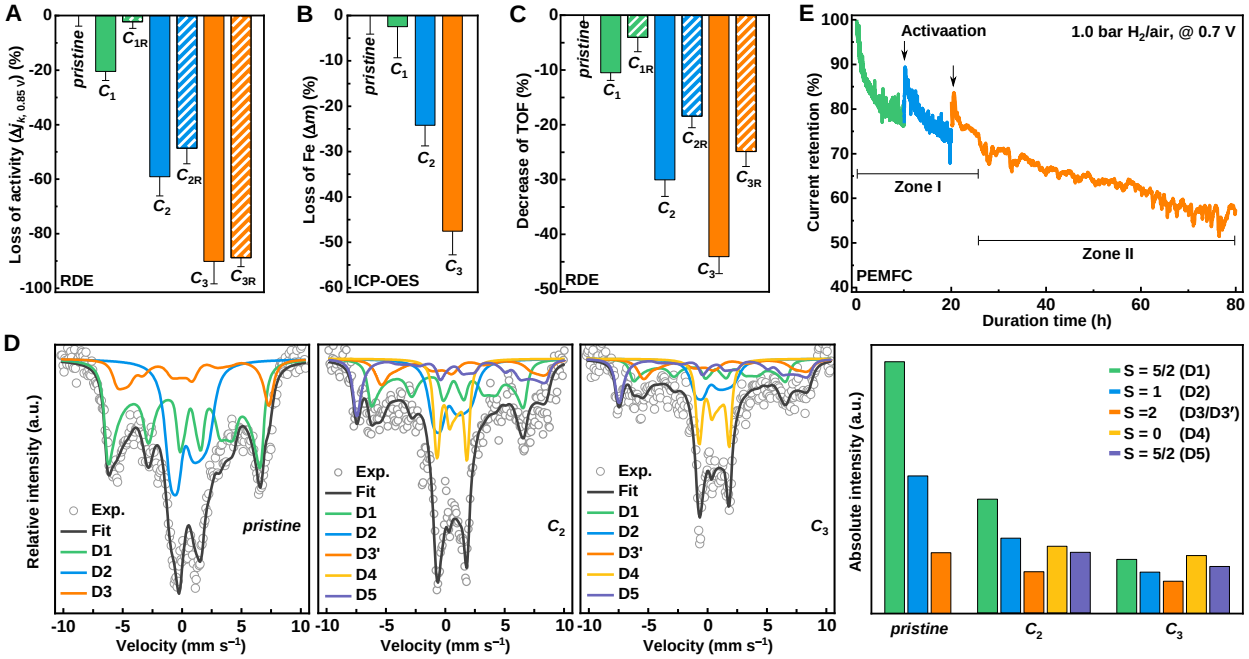

Figure 3 (A-C) relative loss of catalytic activity (i.e., $\Delta j_{k,\ 0.85\ V}$) (A), Fe (B), and TOF (C) of Fe-N-C-600 after the ex situ treatments. The error bars represent the S.D. for three independent experiments performed under the given conditions. (D) ^{57}Fe Mössbauer spectra of the *pristine*, C_2, and C_3 catalysts (measured with an EMF of 7 T) and absolute intensity of each fitted spectral component. (E) H_2/air PEMFC stability of Fe-N-C-600 at 0.7 V. Cathode: 2.5 mg cm$^{-2}_{\text{Fe-N-C-600}}$, anode: 0.1 mg cm$^{-2}_{\text{Pt}}$, 5.0 cm^2 MEA, NR211 membrane, 1.0 bar H_2/air, 80 °C, and 100% RH.

ICP-OES analysis reveals that the Δm for C_1 is only –2.5% (Figure 3B), confirming FeN_xC_y sites in Fe-N-C-600 remain largely stable in Ar-saturated H_2SO_4. An analysis of the Fe site density (SD) of catalysts confirms that the Fe SD for C_1 is nearly unchanged (Figures S24 and S25), which, in combination with the fact that the TOF of C_1 decreased (Figures 3C and S25), indicates that the activity loss of C_1 is primarily due to the decrease in catalytic ORR TOF. For C_2, the Δm increases to –24.2%, and for C_3, it further rises to –47.5%. These findings shows that O_2 exposure contributes to the demetallation of FeN_xC_y sites that are otherwise stable under inert

(i.e., acidic-environment) condition and ROS further demetallizes FeN_xC_y sites that are stable under O_2.

To distinguish the effects of carbon oxidation and demetallation on the ORR catalytic activity in acidic-environment, O_2, and O_2 + ROS, we performed in situ activity recovery RDE tests on C_1, C_2, and C_3. This process electrochemically removes the surface O functionalities (Figures S23 and S25),[26, 47] and the recovered electrodes are designated as C_{1R}, C_{2R}, and C_{3R}, respectively. As shown in Figure 3A, the activity ($j_{k,\ 0.85\ V}$) recovery is substantial for C_{1R}, confirming that the activity loss under acidic-environment is caused mainly by decrease of TOF,[26] rather than by the loss of Fe. In contrast, the amount of activity recovery is minimal for C_{2R} and negligible for C_{3R}, respectively. This is due to the severe destruction, i.e., demetallation, of the FeN_xC_y sites under O_2 or O_2 + ROS, preventing recovery of activity despite some improvements in TOF for the remaining FeN_xC_y sites (Figure 3C). Therefore, although carbon oxidation plays a role in Fe-N-C degradation under these conditions, FeN_xC_y demetallation emerges as the primary mechanism for Fe-N-C degradation with the existence of O_2 or O_2 +ROS. This is further supported by the well-matched trend observed with Δj_k and Δm for catalysts C_1-C_3.

Catalysts C_2 and C_3 were further characterized using cryogenic ^{57}Fe Mössbauer spectroscopy. Five spectral components were needed to appropriately fit their spectra with an external magnetic field (EMF) of 7 T, including the three spectral components D1, D2, and D3 adopted for the fitting of Fe-N-C-600 and two additional components D4 and D5 (Figures 3D and S8). Components D1 (Fe S1 sites) and D2 (Fe S2 sites) are identical across all catalysts, while D3, assigned to high-spin Fe^{2+} species, has slightly different parameters for C_2 and C_3 compared to fresh Fe-N-C-600 catalyst, and it is therefore labelled as D3' in C_2 and C_3 (Table S3). Components D4 and D5 can be assigned to atomically dispersed low-spin (LS) Fe^{2+} and high-spin (HS) Fe^{3+} species, respectively, based on their isomer shifts and hyperfine field splitting values. They may be assigned to modified FeN_xC_y environment relative to D1 and D2, respectively, possibly resulting from formation of functional groups next to FeN_4 sites. Similar D4 and D5 components have also been identified by cryo ^{57}Fe Mössbauer spectroscopy under EMF for an single atom Fe-N-C catalyst prepared by Mg-Fe metal-exchange.[48] A comparison of the absolute signal intensities for the spectral components across all the catalysts identifies that the intensities of S1 (i.e., D1) and S2 (i.e., D2) decrease gradually, with S1 losing more intensity than S2 (see column figure in Figure 3D) (note that the amount of catalyst used for the Mössbauer analyses was consistent across catalysts (within ±4% experimental error)). Notably, the absolute intensities of D4 and D5 did not increase from C_2 to C_3, suggesting that the presence of O_2 + ROS enhanced the destruction of S1 and S2 sites, resulting in Fe dissolution from catalysts. In contrast, exposure to O_2 only led to modification of S1 and S2 without their complete destruction, resulting in the formation of new components D4 and D5. The total signal intensity of all components decreases from Fe-N-C-600 to C_2 and C_3, in line with the reduction in Fe content determined with ICP-OES and nitrite stripping (Table S5).

Upon further inspection of Figure 2D, it is now possible to distinguish the degradation of Fe-N-C and its dependence on the key stability stressors at different stages of decay (Figure S26). As shown in Figures 3E and S27, in the initial rapid activity loss phase (Zone I), a recovery voltage (e.g., 0.05 V versus RHE, 5 minutes) applied to the Fe-N-C-600 cathode led to certain recovery of the activity. Similar recoveries have also been reported in the literature for atomic Fe-N-C catalysts in RDE and PEMFC measurements (Figure S28). This observation shows that Fe-N-C degradation involves a complex interplay between local carbon oxidation induced by the acidic-environment, O_2, and ROS, as well as demetallation driven by O_2 + ROS. We note that the

specific degradation mechanisms for different Fe-N-C catalysts — whether local carbon oxidation or Fe demetallation — depend on the chemistry and structure of the Fe-N-C catalysts. In the subsequent degradation phase (i.e., Zone II), while carbon oxidation continues, albeit at relatively slower rate due to prior oxidation in Zone I, the primary degradation mechanism shifts to the demetallation of the FeN_xC_y active sites, driven by O_2 + ROS. Our in situ CO_2 emission tests also excluded irreversible carbon oxidation (i.e., direct oxidation to CO_2) as a significant contributor to Fe-N-C catalyst degradation under given conditions (Figure S29).

2.3. DFT Calculations

To simulate local carbon oxidation, we constructed various computational structures with an O or OH attached to a carbon atom adjacent to S1 or S2 site and designated these structures as S1-O, S1-OH, S2-O, and S2-OH (Figures 4A, S30, and S31). We predicted the thermodynamic free-energy evolution through $4e^-$ associative ORR pathways on S1, S1-O, S1-OH, S2, S2-O, and S2-OH using the computational hydrogen electrode method.[49] The results reveal that all the FeN_x sites can bind the oxygen intermediates appropriately to complete the ORR (Table S6). Figure 4B and 4C shows that the free-energy change for the elementary steps of the ORR with S1, S1-O, S1-OH, S2, S2-O, and S2-OH are negative (i.e., exergonic) when the electrode potential (U) is lower than the corresponding limiting potential[50] of 0.71, 0.58, 0.7, 0.63, 0.85, and 0.51 V, respectively. Thus, all the FeN_4 sites are predicted to be thermodynamically capable of electrocatalyzing ORR through $4e^-$ pathway. In addition, the activation energy (E_a) required for OOH dissociation (Figure S32), are predicted to be 0.71, 0.72, and 0.59 eV on S1, S1-OH, and S2, respectively. In contrast, S1-O, S2-O, and S2-OH, require higher E_a of 0.98, 1.09, and 1.01 eV, respectively, to dissociate OOH. The above results reveal that the presence of the OH group has minimal effect on the ORR activity (i.e., TOF) of S1, but it decreases the activity of S2. Meanwhile, O adsorbate reduces the activity of both S1 and S2.

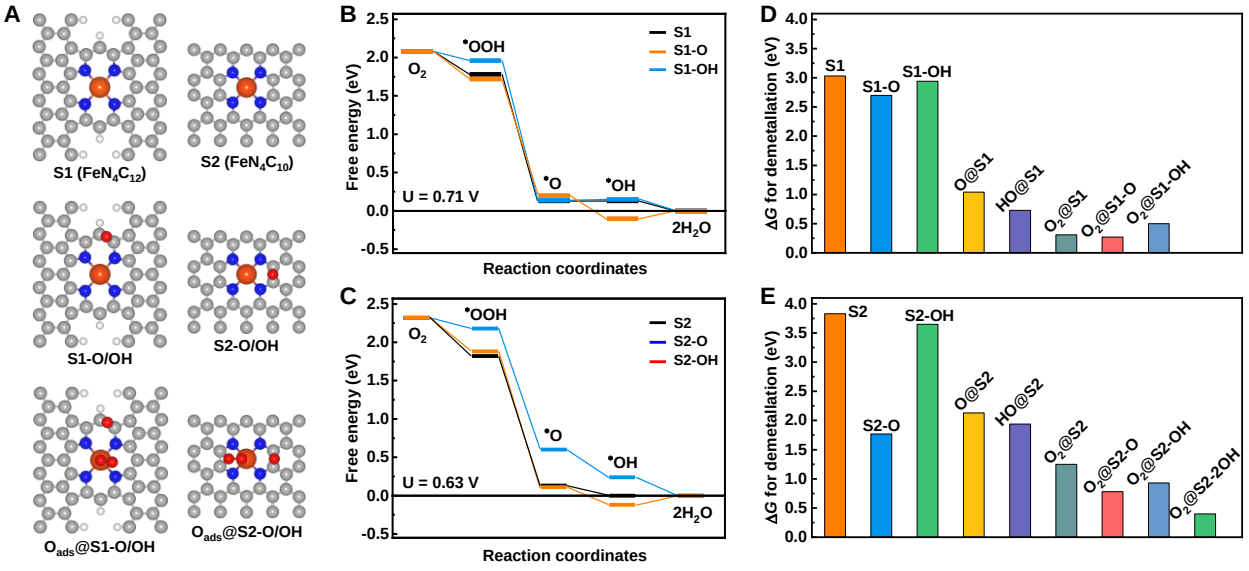

Figure 4 (A) Atomistic structures of S1 and S2, S1- or S2-O/OH and O_{ads}@S1- or O_{ads}@S2-O/OH (ads: O_2, O, or OH). In the figure, the grey, blue, orange, red, and white represent C, N, Fe, O, and H atoms, respectively. (B) and (C) Predicted free-energy evolution for the ORR via $4e^-$ associative pathway on (B) S1, S1-O, and S1-OH sites under 0.71 V electode potential (U) and (C) S2, S2-O, and S2-OH sites under 0.63 V electrode potential. The asterisk denotes the adsorption sites. (D) and (E) Predicted ΔG for demetallation of S1 (D) and S2 (E) sites without, with O or OH, and with O_2 or O_2-O/OH adsorbates. Higher positive ΔG value indicates higher resistance against the demetallation.

To better understand the stability of the Fe-N-C catalysts and the influence of the key stability stressors, we then performed the spin-polarized density functional theory (SP-DFT) simulations to assess the tendency for demetallation, focusing on the role of O_2 and ROS. We simulated the Gibbs free energy change (ΔG) for demetallation of S1 and S2 sites under some representative scenarios: (1) S1 and S2 without adsorbates, (2) adsorption of O or OH ($^{\bullet}$O or $^{\bullet}$OH from H_2O_2 and *O or *OH from ORR) on C adjacent to FeN_4 (e.g., S1-O, S1-OH, S2-O, and S2-OH), (3) adsorption of O_2 on Fe (e.g., O_2@S1 and O_2@S2), and (4) coadsorption of O_2-O and O_2-OH on Fe-C (e.g., O_2@S1-O, O_2@S1-OH, O_2@S2-O, and O_2@S2-OH) (Figures 4A and S33). The simulations indicate that S1 and S2, in the absence of adsorbates, require a ΔG larger than 3.0 eV for the demetallation (Figure 4D and 4E), which shows that they are structurally stable under these conditions. This is consistent with our ex situ experiment results under deaerated condition. When an O or OH is added onto the C near FeN_4 site, the ΔG values for demetallation of S1 and S2 decrease but remain above 1.7 eV. For the sites where O_2 is directly adsorbed on Fe, the ΔG for the demetallation process is calculated to be only 0.31 eV for O_2@S1 but nearly 1.25 eV for O_2@S2, implying that, from a thermodynamic perspective,[51] O_2 promote the demetallation of S1 but not S2 site. Moreover, we calculated the ΔG values for the coadsorption of O_2-O/OH on S1 and S2: 0.27, 0.5, 0.78, and 0.93 eV for O_2@S1-O, O_2@S1-OH, O_2@S2-O, and O_2@S2-OH, respectively. This suggests that both S1 and S2 sites are unstable under such a coadsorption condition. We note that although neither S1 nor S2 are stable with O_2 or O_2-O or O_2-OH adsorptions, the tendency for demetallation of S1 is higher than that of S2 under O_2 or O_2-O/O_2-OH (i.e., O_2 + ROS) conditions. The ΔG for O_2@S2-OH further decreases to 0.40 eV when adding another OH onto the C adjacent to S2, indicating that S2 becomes even more unstable with a high concentration of OH (i.e., ROS). Our computational findings align with the ^{57}Fe Mössbauer spectral results, which reveal that although S2 is more stable than S1 with key ORR stability stressors, it is not stable enough under high ROS concentration conditions.

3. CONCLUSION

In this work, we investigated the complex degradation mechanisms behind single atomic Fe-N-C catalyst. We identified that the oxidation of local carbon, driven by key stability stressors, i.e., the acidic-environment, O_2, and ROS, along with the demetallation of FeN_xC_y active sites by O_2 + ROS, are the primary causes of the initial fast degradation of Fe-N-C. Demetallation of the FeN_xC_y active sites by O_2 or O_2 + ROS is primarily responsible for the subsequent slow degradation of Fe-N-C. Similar degradation behavior can be observed for the Fe-N-C-Δ and our previously reported Mn-N-C[52] catalysts (Figure S34). These findings show that the degradation of Fe-N-C for the ORR involves a complex interplay between mainly FeN_xC_y local carbon oxidation (Figure S35) and Fe demetallation. This is different from earlier research results that the degradation of Fe-N-C can be primarily ascribed to either carbon oxidation[16-18, 25, 26, 53] or FeN_xC_y sites demetallation[19, 21-23, 29, 54-56]. Therefore, besides constructing more stable FeN_xC_y sites (e.g., S2[30, 31], Pt-FeN_xC_y[29]), regulating FeN_x surrounding environment to prevent local carbon oxidation, that is, to alleviate or circumvent the decreasing of FeN_xC_y sites ORR TOF, is crucial for improving the stability of Fe-N-C catalysts. Moreover, we observed that S1 active sites are more prone to demetallation than S2 sites under O_2 or O_2 + ROS conditions. These findings show the primary reason for why S1 sites typically exhibit the much easier demetallation than S2 sites, which is a more in-depth understanding of degradation mechanisms of the FeN_xC_y active sites compared with previous studies.[20, 29, 30, 55] This suggest that although an increasing in the content of relatively stable S2 sites enhanced the stability of Fe-N-C

catalysts,[20, 30, 31, 57] mitigating S2 demetallation by ROS is also critically important for maintaining stability of Fe-N-C catalysts.

4. EXPERIMENTAL SECTION

The experimental details ─ including catalyst synthesis, ex situ demetallation experiments, catalyst characterizations, Mössbauer analysis, electrochemical tests, and DFT simulations ─ are described in the Supporting Information.

■ ASSOCIATED CONTENT

The Supporting Information is available free of charge at: xxx xxx

General methods; additional XRD, TEM, HAADF-STEM, XANES, FT-EXAFS, XPS, Mössbauer spectroscopy, nitrogen sorption isotherms and pore size distribution, and electrochemical results; additional simulation results (PDF)

■ AUTHOR INFORMATION

Corresponding Authors

Frédéric Jaouen − *ICGM, University of Montpellier, CNRS, ENSCM, 34293 Montpellier, France;* Email: frederic.jaouen@umontpellier.fr

Lijun Yang − *Ballard Power Systems Inc., Burnaby, BC V5J 5J8, Canada;* Email: lijun.yang@ballard.com

Guofeng Wang − *Department of Mechanical Engineering and Materials Science, University of Pittsburgh, Pittsburgh, Pennsylvania 15260, United States;* Email: guw8@pitt.edu

Yuyan Shao − *Energy and Environment Directorate, Pacific Northwest National Laboratory, Richland, Washington 99354, United States;* Email: yuyan.shao@pnnl.gov

Authors

Xiaohong Xie − *Energy and Environment Directorate, Pacific Northwest National Laboratory, Richland, Washington 99354, United States; Present Address: State Key Laboratory of Advanced Chemical Power Sources, School of Chemistry and Chemical Engineering, Chongqing University, Chongqing 400044, China*

Boyang Li − *Department of Mechanical Engineering and Materials Science, University of Pittsburgh, Pittsburgh, Pennsylvania 15260, United States*

Pan Xu − *Ballard Power Systems Inc., Burnaby, BC V5J 5J8, Canada*

Moulay Tahar Sougrati − *ICGM, University of Montpellier, CNRS, ENSCM, 34293 Montpellier, France*

Ricardo Garcia-Serres − *Université Grenoble Alpes, CNRS, CEA, IRIG, Laboratoire de Chimie et Biologie des Métaux,17 Rue Des Martyrs, 38000, Grenoble, France*

David A. Cullen − *Center for Nanophase Materials Sciences, Oak Ridge National Laboratory, Oak Ridge, Tennessee 37831, United States*

A. Jeremy Kropf − *Chemical Sciences and Engineering Division, Argonne National Laboratory, Lemont, Illinois 60439, United States*

Fan Xia − *Department of Chemistry and Biochemistry, Northern Illinois University, DeKalb, Illinois 60115, United States*

Miao Song − *Physical and Computational Sciences Directorate, Pacific Northwest National Laboratory, Richland, Washington 99354, United States*

Sulay Saha − *Department of Energy, Environmental and Chemical Engineering, Washington University in St. Louis, St. Louis, Missouri 63130, United States*

Yachao Zeng − *Department of Chemical and Biological Engineering, University at Buffalo, The State University of New York, Buffalo, New York 14260, United States*

Mark H. Engelhard − *Physical and Computational Sciences Directorate, Pacific Northwest National Laboratory, Richland, Washington 99354, United States*

Mark E. Bowden − *Physical and Computational Sciences Directorate, Pacific Northwest National Laboratory, Richland, Washington 99354, United States*

Hanguang Zhang − *Materials Physics and Applications Division, Los Alamos National Laboratory, Los Alamos, New Mexico 87545, United States*

Litao Yan − *Energy and Environment Directorate, Pacific Northwest National Laboratory, Richland, Washington 99354, United States*

Teresa Lemmon − *Energy and Environment Directorate, Pacific Northwest National Laboratory, Richland, Washington 99354, United States*

Xiaohong S. Li − *Energy and Environment Directorate, Pacific Northwest National Laboratory, Richland, Washington 99354, United States*

Ulises Martinez − *Materials Physics and Applications Division, Los Alamos National Laboratory, Los Alamos, New Mexico 87545, United States*

Yingwen Cheng − *Department of Chemistry and Biochemistry, Northern Illinois University, DeKalb, Illinois 60115, United States*

Gang Wu − *Department of Energy, Environmental and Chemical Engineering, Washington University in St. Louis, St. Louis, Missouri 63130, United States*

Piotr Zelenay − *Materials Physics and Applications Division, Los Alamos National Laboratory, Los Alamos, New Mexico 87545, United States*

Vijay Ramani − *Department of Energy, Environmental and Chemical Engineering, Washington University in St. Louis, St. Louis, Missouri 63130, United States*

Deborah J. Myers − *Chemical Sciences and Engineering Division, Argonne National Laboratory, Lemont, Illinois 60439, United States*

Complete contact information is available at: xxx xxx

Author Contributions

[§]X.X., B.L., and P.X. contributed equally to this work.

Notes

The authors declare no competing financial interest.

■ ACKNOWLEDGEMENTS

The authors acknowledge support from the U.S. Department of Energy (DOE), Energy Efficiency and Renewable Energy, Hydrogen and Fuel Cell Technologies Office through the Electrocatalysis consortium (ElectroCat) and the DOE program managers, Gregory Kleen, David Peterson, Simon Thompson, Dimitrios Papageorgopoulos. The XPS measurement was conducted at the William R. Wiley Environmental Molecular Sciences Laboratory (EMSL), a national scientific user facility at Pacific Northwest National Laboratory (PNNL) which is sponsored by DOE's Office of Biological and Environmental Research (BER). PNNL is operated by Battelle for the US DOE under Contract DE-AC05-76RLO1830. X-ray spectroscopy analysis were

carried out at MRCAT at the Advanced Photon Source (APS), an Office of Science user facility operated for the DOE's Office of Science by Argonne National Laboratory (ANL) under Contract DE-AC02-06CH11357. The operation of MRCAT is supported both by DOE and the MRCAT member institutions. ANL is operated for the US DOE by UChicago Argonne LLC under Contract DE-AC02-06CH11357. Electron microscopy research of material was conducted as a part of a user project at the Center for Nanophase Materials Sciences (CNMS), a DOE's Office of Science user facility at Oak Ridge National Laboratory. The Spin-polarized DFT calculations were performed on the computers of the University of Pittsburgh Center for Research Computing (CRC) as well as the Extreme Science and Engineering Discovery Environment (XSEDE), which is funded by the National Science Foundation (NSF) grant number ACI-1053575. Cryogenic Mössbauer characterization received funding from the French National Research Agency (Labex ARCANE, CBH-EUR-GS, ANR-17-EURE-0003).

■ REFERENCES

1. Yang, G.Q. et al. Advanced electrode structures for proton exchange membrane fuel cells: current status and path forward. *Electrochem. Energy Rev.* **7**, 9 (2024).
2. Jiao, K. et al. Designing the next generation of proton-exchange membrane fuel cells. *Nature* **595**, 361-369 (2021).
3. Liu, Z.Y. et al. Pt catalyst protected by graphene nanopockets enables lifetimes of over 200,000 h for heavy-duty fuel cell applications. *Nat. Nanotechnol.* **20**, 807-814 (2025).
4. Thompson, S.T. et al. Direct hydrogen fuel cell electric vehicle cost analysis: System and high-volume manufacturing description, validation, and outlook. *J. Pow. Sour.* **399**, 304-313 (2018).
5. Chung, H.T. et al. Direct atomic-level insight into the active sites of a high-performance PGM-free ORR catalyst. *Science* **357**, 479-483 (2017).
6. Lefèvre, M., Proietti, E., Jaouen, F. & Dodelet, J.P. Iron-based catalysts with improved oxygen reduction activity in polymer electrolyte fuel cells. *Science* **324**, 71-74 (2009).
7. Wan, X. et al. Fe-N-C electrocatalyst with dense active sites and efficient mass transport for high-performance proton exchange membrane fuel cells. *Nat. Catal.* **2**, 259-268 (2019).
8. Zhang, H.G. et al. Single atomic iron catalysts for oxygen reduction in acidic media: Particle size control and thermal activation. *J. Am. Chem. Soc.* **139**, 14143-14149 (2017).
9. He, Y.H. & Wu, G. PGM-free oxygen-reduction catalyst development for proton-exchange membrane fuel cells: challenges, solutions, and promises. *Acc. Mater. Res.* **3**, 224-236 (2022).
10. Shao, Y.Y., Dodelet, J.P., Wu, G. & Zelenay, P. PGM-free cathode catalysts for PEM fuel cells: A mini-review on stability challenges. *Adv. Mater.* **31**, 1807615 (2019).
11. Du, L. et al. Low-PGM and PGM-free catalysts for proton exchange membrane fuel cells: stability challenges and material solutions. *Adv. Mater.* **33**, 1908232 (2021).
12. He, Y.H., Liu, S.W., Priest, C., Shi, Q.R. & Wu, G. Atomically dispersed metal-nitrogen-carbon catalysts for fuel cells: advances in catalyst design, electrode performance, and durability improvement. *Chem. Soc. Rev.* **49**, 3484-3524 (2020).
13. Uddin, A. et al. High power density platinum group metal-free cathodes for polymer electrolyte fuel cells. *ACS Appl. Mater. Inter.* **12**, 2216-2224 (2020).
14. Jiao, L. et al. Chemical vapour deposition of Fe-N-C oxygen reduction catalysts with full utilization of dense Fe-N_4 sites. *Nat. Mater.* **20**, 1385-1391 (2021).
15. Zhang, H.G. et al. High-performance fuel cell cathodes exclusively containing atomically dispersed iron active sites. *Energy Environ. Sci.* **12**, 2548-2558 (2019).
16. Kumar, K. et al. On the Influence of oxygen on the degradation of Fe-N-C catalysts. *Angew. Chem. Int. Ed.* **59**, 3235-3243 (2020).

17. Kumar, K. et al. Physical and chemical considerations for improving catalytic activity and stability of non-precious-metal oxygen reduction reaction catalysts. *ACS Catal.* **8**, 11264-11276 (2018).
18. Choi, C.H. et al. Stability of Fe-N-C catalysts in acidic medium studied by operando spectroscopy. *Angew. Chem. Int. Edit.* **54**, 12753-12757 (2015).
19. Chenitz, R. et al. A specific demetalation of Fe-N_4 catalytic sites in the micropores of NC_Ar + NH_3 is at the origin of the initial activity loss of the highly active Fe/N/C catalyst used for the reduction of oxygen in PEM fuel cells. *Energy Environ. Sci.* **11**, 365-382 (2018).
20. Li, J.K. et al. Identification of durable and non-durable FeN_x sites in Fe-N-C materials for proton exchange membrane fuel cells. *Nat. Catal.* **4**, 10-19 (2021).
21. Xie, X.H. et al. Performance enhancement and degradation mechanism identification of a single-atom Co-N-C catalyst for proton exchange membrane fuel cells. *Nat. Catal.* **3**, 1044-1054 (2020).
22. Pedersen, A. et al. Fe dissolution in Fe-N-C electrocatalysts during acidic oxygen reduction: impact of local pH change. *Energ Environ Sci* **17**, 6323-6337 (2024).
23. Chen, W.W. et al. Degradation of FeNC electrocatalysts for acidic and alkaline oxygen reduction. *J. Am. Chem. Soc.* **147**, 35730-35741 (2025).
24. Herranz, J. et al. Unveiling N-protonation and anion-binding effects on Fe/N/C catalysts for O_2 reduction in proton-exchange-membrane fuel cells. *J. Phys. Chem. C* **115**, 16087-16097 (2011).
25. Yin, X. & Zelenay, P. Kinetic models for the degradation mechanisms of PGM-free ORR catalysts. *ECS Trans.* **85**, 1239-1250 (2018).
26. Choi, C.H. et al. The Achilles' heel of iron-based catalysts during oxygen reduction in an acidic medium. *Energy Environ. Sci.* **11**, 3176-3182 (2018).
27. Banham, D. et al. Critical advancements in achieving high power and stable nonprecious metal catalyst-based MEAs for real-world proton exchange membrane fuel cell applications. *Sci. Adv.* **4**, eaar7180 (2018).
28. Gubler, L., Dockheer, S.M. & Koppenol, W.H. Radical ($HO^{\bullet}$, $H^{\bullet}$ and $HOO^{\bullet}$) formation and ionomer degradation in polymer electrolyte fuel cells. *J. Electrochem. Soc.* **158**, B755-B769 (2011).
29. Bae, G. et al. Unravelling the complex causality behind Fe-N-C degradation in fuel cells. *Nat. Catal.* **6**, 1140-1150 (2023).
30. Liu, S.W. et al. Atomically dispersed iron sites with a nitrogen-carbon coating as highly active and durable oxygen reduction catalysts for fuel cells. *Nat. Energy* **7**, 652-663 (2022).
31. Zeng, Y.C. et al. Tuning the thermal activation atmosphere breaks the activity-stability trade-off of Fe-N-C oxygen reduction fuel cell catalysts. *Nat. Catal.* **6**, 1215-1227 (2023).
32. Liu, Y.H. et al. Progress and challenges in structural, and characterization of single-atom catalysts by X-ray based synchrotron radiation techniques. *Chem. Soc. Rev.* **53** (2024).
33. Li, J.K. et al. Structural and mechanistic basis for the high activity of Fe-N-C catalysts toward oxygen reduction. *Energy Environ. Sci.* **9**, 2418-2432 (2016).
34. Zitolo, A. et al. Identification of catalytic sites for oxygen reduction in iron- and nitrogen-doped graphene materials. *Nat. Mater.* **14**, 937-942 (2015).
35. Li, J.K. et al. Evolution pathway from iron compounds to Fe(II)-N_4 sites through gas-phase iron during pyrolysis. *J. Am. Chem. Soc.* **142**, 1417-1423 (2020).
36. Jin, Z.Y. et al. Understanding the inter-site distance effect in single-atom catalysts for oxygen electroreduction. *Nat. Catal.* **4**, 615-622 (2021).
37. Zhang, Z.P., Sun, J.T., Wang, F. & Dai, L.M. Efficient oxygen reduction reaction (ORR) catalysts based on single iron atoms dispersed on a hierarchically structured porous carbon framework. *Angew. Chem. Int. Edit.* **57**, 9038-9043 (2018).
38. Mehmood, A. et al. High loading of single atomic iron sites in Fe-NC oxygen reduction catalysts for proton exchange membrane fuel cells. *Nat. Catal.* **5**, 311-323 (2022).

39. Choi, C.H. et al. Unraveling the nature of sites active toward hydrogen peroxide reduction in Fe-N-C catalysts. *Angew. Chem. Int. Ed.* **56**, 8809-8812 (2017).
40. Bonakdarpour, A. et al. Impact of loading in RRDE experiments on Fe-N-C catalysts: Two- or four-electron oxygen reduction? *Electrochem. Solid-State Lett.* **11**, B105-B108 (2008).
41. Zhang, H.G. et al. Standardized protocols for evaluating platinum group metal-free oxygen reduction reaction electrocatalysts in polymer electrolyte fuel cells. *Nat. Catal.* **5**, 455-462 (2022).
42. Yu, S.R., Levell, Z., Jiang, Z., Zhao, X.H. & Liu, Y.Y. What is the rate-limiting step of oxygen reduction reaction on Fe-N-C catalysts? *J. Am. Chem. Soc.* **145**, 25352-25356 (2023).
43. Li, J.K., Alsudairi, A., Ma, Z.F., Mukerjee, S. & Jia, Q.Y. Asymmetric volcano trend in oxygen reduction activity of Pt and non-Pt catalysts: *In situ* identification of the site-blocking effect. *J. Am. Chem. Soc.* **139**, 1384-1387 (2017).
44. Cruz-Manzo, S., Chen, R. & Rama, P. Study of current distribution and oxygen diffusion in the fuel cell cathode catalyst layer through electrochemical impedance spectroscopy. *Int. J. Hydrogen Energ.* **38**, 1702-1713 (2013).
45. Banham, D. et al. New insights into non-precious metal catalyst layer designs for proton exchange membrane fuel cells: Improving performance and stability. *J. Power Sources* **344**, 39-45 (2017).
46. Sassin, M.B., Garsany, Y., Atkinson, R.W., Hjelm, R.M.E. & Swider-Lyons, K.E. Understanding the interplay between cathode catalyst layer porosity and thickness on transport limitations en route to high-performance PEMFCs. *Int. J. Hydrogen Energy* **44**, 16944-16955 (2019).
47. Beltrán, D.E. et al. Elucidation of performance recovery for Fe-based catalyst cathodes in fuel cells. *Adv. Energy Sustainability Res.* **2**, 2100123 (2021).
48. Barrio, J. et al. FeNC oxygen reduction electrocatalyst with high utilization penta-coordinated sites. *Adv. Mater.* **35**, 2211022 (2023).
49. Norskov, J.K. et al. Origin of the overpotential for oxygen reduction at a fuel-cell cathode. *J. Phy. Chem. B* **108**, 17886-17892 (2004).
50. Kulkarni, A., Siahrostami, S., Patel, A. & Norskov, J.K. Understanding catalytic activity trends in the oxygen reduction reaction. *Chem. Rev.* **118**, 2302-2312 (2018).
51. Nørskov, J.K., Studt, F., Abild-Pedersen, F. & Bligaard, T. *Fundamental Concepts in Heterogeneous Catalysis*. (John Wiley and Sons, 2014).
52. Li, J.Z. et al. Atomically dispersed manganese catalysts for oxygen reduction in proton-exchange membrane fuel cells. *Nat. Catal.* **1**, 935-945 (2018).
53. Lefèvre, M. & Dodelet, J.P. Fe-based catalysts for the reduction of oxygen in polymer electrolyte membrane fuel cell conditions: determination of the amount of peroxide released during electroreduction and its influence on the stability of the catalysts. *Electrochim. Acta* **48**, 2749-2760 (2003).
54. Chen, J.R. et al. Insight into the rapid degradation behavior of nonprecious metal Fe-N-C electrocatalyst-based proton exchange membrane fuel cells. *ACS Appl. Mater. Interfaces* **11**, 37779-37786 (2019).
55. Xu, X.L. et al. Investigation on the demetallation of Fe-N-C for oxygen reduction reaction: The influence of structure and structural evolution of active site. *Appl. Catal. B Environ.* **309** (2022).
56. Santori, P.G. et al. Effect of pyrolysis atmosphere and electrolyte pH on the oxygen reduction activity, stability and spectroscopic signature of FeN_x moieties in Fe-N-C catalysts. *J. Electrochem. Soc.* **166** (2019).
57. Wu, G. & Zelenay, P. Activity versus stability of atomically dispersed transition-metal electrocatalysts. *Nat. Rev. Mater.* **9**, 643-656 (2024).

TOC Graphic:

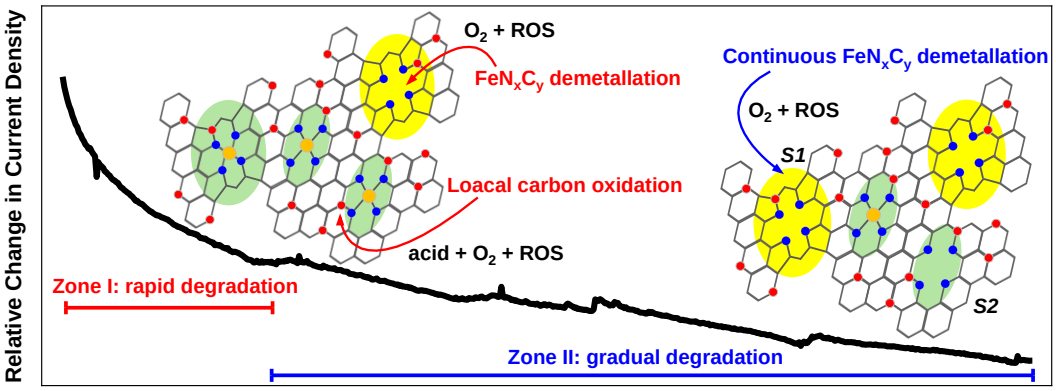
Relative Change in Current Density
O_2 + ROS
FeN_xC_y demetallation
Loacal carbon oxidation
acid + O_2 + ROS
Zone I: rapid degradation
Continuous FeN_xC_y demetallation
O_2 + ROS
S1
S2
Zone II: gradual degradation